Materials Science & Engineering A 575 (2013) 41–47

Contents lists available at SciVerse ScienceDirect

Materials Science & Engineering A

journal homepage: www.elsevier.com/locate/msea

Effect of hot deformation mode on the microstructure evolution of lean duplex stainless steel 2101

Yanyan Liu [a], Haitao Yan [b], Xinhua Wang [a], Mi Yan [a,*]

[a] State Key Laboratory of Silicon Materials, Department of Materials Science and Engineering, Zhejiang University, Hangzhou 310027, PR China
[b] DongFang Special Steel Co. Ltd, Jiaxing 314000, PR China

ARTICLE INFO

Article history:
Received 6 December 2012
Received in revised form
15 March 2013
Accepted 19 March 2013
Available online 27 March 2013

Keywords:
Lean duplex stainless steel 2101
Multi-pass hot deformation
EBSD
Texture

ABSTRACT

Microstructure and crystallographic texture evolution of lean duplex stainless steel 2101 (LDX 2101) during single- and multi-pass hot compressions were studied by electron backscatter diffraction (EBSD). The flow curve characteristics of LDX 2101 were interpreted by coupling behaviors of the microstructure evolution in austenitic and ferric phases. The softening of both the phases during straining is caused by continuous dynamic recrystallization by the gradual transformation of low-angle grain boundaries into high-angle grain boundaries, without obvious changes in the phase ratio. The hot compression textures of the constituent phases show that the brass-type texture, which is typical of face-centered cubic materials with low stacking fault energy, is developed in the austenitic phase, and the rotated-cube texture is developed in the ferric phase. The differences in the microstructures and texture evolution features under different hot deformation modes can be explained by the differences in softening mechanisms.

1. Introduction

Duplex stainless steel (DSS) is characterized by a dual phase structure comprising a mixture of ferric and austenitic phases. DSS is increasingly employed in chemical, petrochemical, nuclear, marine, and paper industries primarily because of its excellent mechanical properties and corrosion performance [1].

DSS can be processed through different procedures, such as casting, forging, extrusion or rolling. These procedures are usually performed at high temperatures where the DSS still possesses a duplex structure. However, the different thermal deformation behavior coefficients of each constituent phase (austenite or ferrite) are considerably affected by the presence of the other phase under hot working conditions, which leads to edge cracks or inappropriate surface finish [2].

In hot working operations such as rolling, the schedules of deformation consist of a series of deformation passes and holding times. During this hot working sequence, dynamic and static recovery and recrystallization occur in the two ductile phases, ferrite and austenite. The effects of dynamic and static recovery and recrystallization on ferric or austenitic single-phase materials have been extensively studied by numerous researchers. During hot working, the two major mechanisms of restoration of metals are dynamic recovery (DRV) and dynamic recrystallization (DRX), wherein the stacking fault energy (SFE) determines which mechanism will take place. Single-phase austenitic stainless steels usually undergo DRX because of their low SFE, whereas ferric stainless steels more likely undergo DRV because of their relatively high SFE [2,3].

However, the simultaneous presence of both phases in DSS makes the situation more complex. Only a few reports that deal with high-temperature deformation of DSS and controversial results about the austenitic/ferric phase behavior are available. Dehghan-Manshadi and Hodgson [4] believe that DRX takes place in the austenitic phase, but Fan et al. suggest that this mechanism is inhibited in these two-phase alloys [5]. Cizek and Wynne [6] described the softening mechanism in the ferric phase as “extended dynamic recovery”, while other researchers called it “continuous recrystallization”. The difference between these two mechanisms is defined in terms of the relative amounts of low- and high-angle boundaries in the microstructure. Thus, studying the thermal deformation behaviors of DSS is very important.

The texture development of rolled and annealed single-phase stainless steels (ferric or austenitic stainless steels) is well known, but the texture evolution in DSS has not yet been systematically investigated. The activity of crystallographic slip during deformation leads to pronounced textures in body-centered cubic (bcc) and face-centered cubic (fcc) metals [7]. Changes in the deformation modes alter these textures. Analysis of the textures in DSS provides valuable information on the hardening and softening mechanisms of DSS.

In our recent work, lean duplex stainless steel (LDX) 2101 with a typical composition of 21.5Cr–5Mn–1.5Ni–0.22N–0.3Mo–0.3Cu has

* Corresponding author. Tel.: +86 571 87952730; fax: +86 571 87952366.
E-mail address: mse_yanmi@zju.edu.cn (M. Yan).

0921-5093/$ - see front matter © 2013 Elsevier B.V. All rights reserved.
http://dx.doi.org/10.1016/j.msea.2013.03.036

been developed to further reduce the cost, especially, in which Mn and N contents were increased to save expensive element Ni [8]. However, basic understanding regarding the design of suitable hot working processes such as hot rolling is still lacking. In this paper, the hot working behavior of this newly developed low-cost DSS was examined by systematic hot compression tests under different deformation modes. This study aims to clarify the microstructure evolution of LDX 2101 under different hot deformation modes, such as the austenite/ferrite ratio and phase morphology, the distribution of misorientation angles, and the crystallographic textures.

2. Experimental procedure

The investigated material was a commercial lean duplex stainless steel, LDX 2101, provided by DongFang Special Steel Co. Ltd., (ZhenShi Group). The nominal chemical composition of the steel was (wt%) 21.43 Cr, 1.62 Ni, 0.27 Mo, 4.87 Mn, 0.42 Si, 0.24 N and the balance Fe. The as-received continuous casting slab of 200 mm of thickness was reheated to 1250 °C for 2 h and subsequently forged to a 40 mm thick slab.

Hot compression tests were conducted on a Gleeble-3500 thermo-mechanical simulator with cylindrical specimens of 10 mm in diameter and 15 mm in height, which is manufactured from the forged slab with the longitudinal axis parallel to the deformation direction.

In order to avoid interferences with precipitation of second phase particles (intermetallics or carbides), specimens were soaked at 1200 °C for 5 min and then cooled down to the test temperature at a cooling rate of 5 °C/s. The schematic diagram of deformation modes being analyzed in this paper is presented in Fig. 1. The samples with the duplex structure were deformed in the temperature range of 1000–1100 °C at a strain rate of 5 s^{-1} to different strains. For multi-pass tests, the specimen was unloaded after the ongoing pass, then cooled to a certain temperature at a cooling rate of 5 °C/s before undergoing the next pass of compression. The true strains of each pass are 0.2, 0.2, 0.2, 0.1 and 0.1. Graphite powder was applied on both contacting surfaces of the specimens to reduce the friction coefficient during hot compression testing. To preserve microstructures developed during hot deformation, samples were quenched immediately after reaching a certain strain level marked in Fig. 1.

The quenched specimens were cut along the longitudinal axis and the microstructure investigation was undertaken on planar sections containing the rolling direction (RD) and normal direction (ND), using the high-resolution EBSD technique. In order to obtain EBSD patterns of good quality, it was important to remove the residual deformation in the surface layer of specimens. The investigated surfaces were first mechanically ground and polished down to 0.5 μm diamond paste, then vibratory polished for 1 h with a solution of 0.05 μm colloidal silica suspension. EBSD study was performed using a JOEL JSM-7600F FESEM, equipped with a HKL Technology EBSD attachment, operated at 20 kV. Orientation mapping was performed on a square grid with a step size of 3 μm, providing information about the phase ratio, grain size, grain boundary characteristics, and crystallographic textures. Crystallographic textures were represented using the orientation distribution function (ODF) in Euler space. The data processing was carried out using the HKL Channel 5 software package.

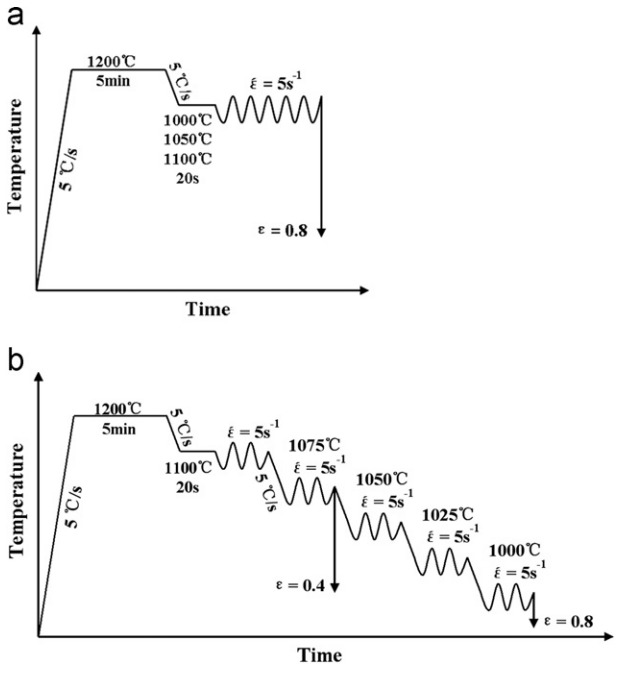

Fig. 1. Schematic diagrams of the deformation modes examined in this work: (a) single-pass mode and (b) multi-pass mode.

3. Results

3.1. Flow curve characteristics

Fig. 2 shows the true stress–true strain flow curves of LDX 2101 during single- and multi-pass hot compressions in the temperature

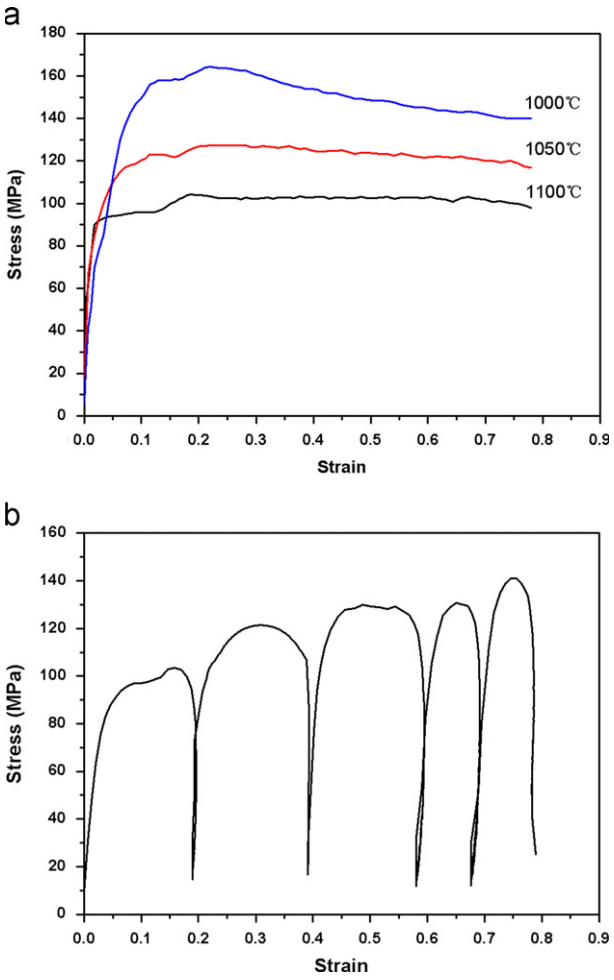

Fig. 2. True stress–true strain curve of LDX 2101 during single- and multi-pass hot compressions: (a) single-pass hot compression and (b) multi-pass hot compression.

range of 1000–1100 °C at a strain rate of 5 s^{-1}. Since the ferric and austenitic phases coexist, coordination deformation occurred in the ferric matrix and austenitic phase. It can be seen from Fig. 2(a) that all the flow curves demonstrate similar characteristics; as strain increases, the single-pass hot compression flow curve shows four stages, namely, strain hardening, "yield point-like" steady softening, strain hardening and softening. It can also be seen that the flow stress increases and the critical strain to the peak stress increases as temperature decreases. For the multi-pass hot compression flow curve, the flow stress rises rapidly to the stress level before unloading after each interrupted period. From the first pass to the last, the stress continues to rise with increasing strain. During the first pass, the flow curve also shows the "yield point-like" steady softening phenomenon, which is similar to the single-pass hot compression flow curve.

3.2. Microstructure evolution

Fig. 3 shows the electron backscatter diffraction (EBSD) images at different strains during single- and multi-pass hot compressions and the corresponding adjacent grain misorientation distribution maps of both the phases. The blue and red areas in EBSD images represent ferric and austenitic phases, respectively. The white thick lines represent ∑3 twin boundary ($\theta=60^\circ$), the black thick lines represent other large-angle grain boundaries (HAGB, $\theta>15^\circ$), and the thin gray lines represent small-angle grain boundaries (LAGB, $\theta\leq15^\circ$).

EBSD analysis results show that the forged plate starting material subjected to preheating at 1050 °C for 30 min contained approximately 49.5% austenitic phase in the form of elongated islands embedded in the coarse-grained ferric matrix (Fig. 3(a)),

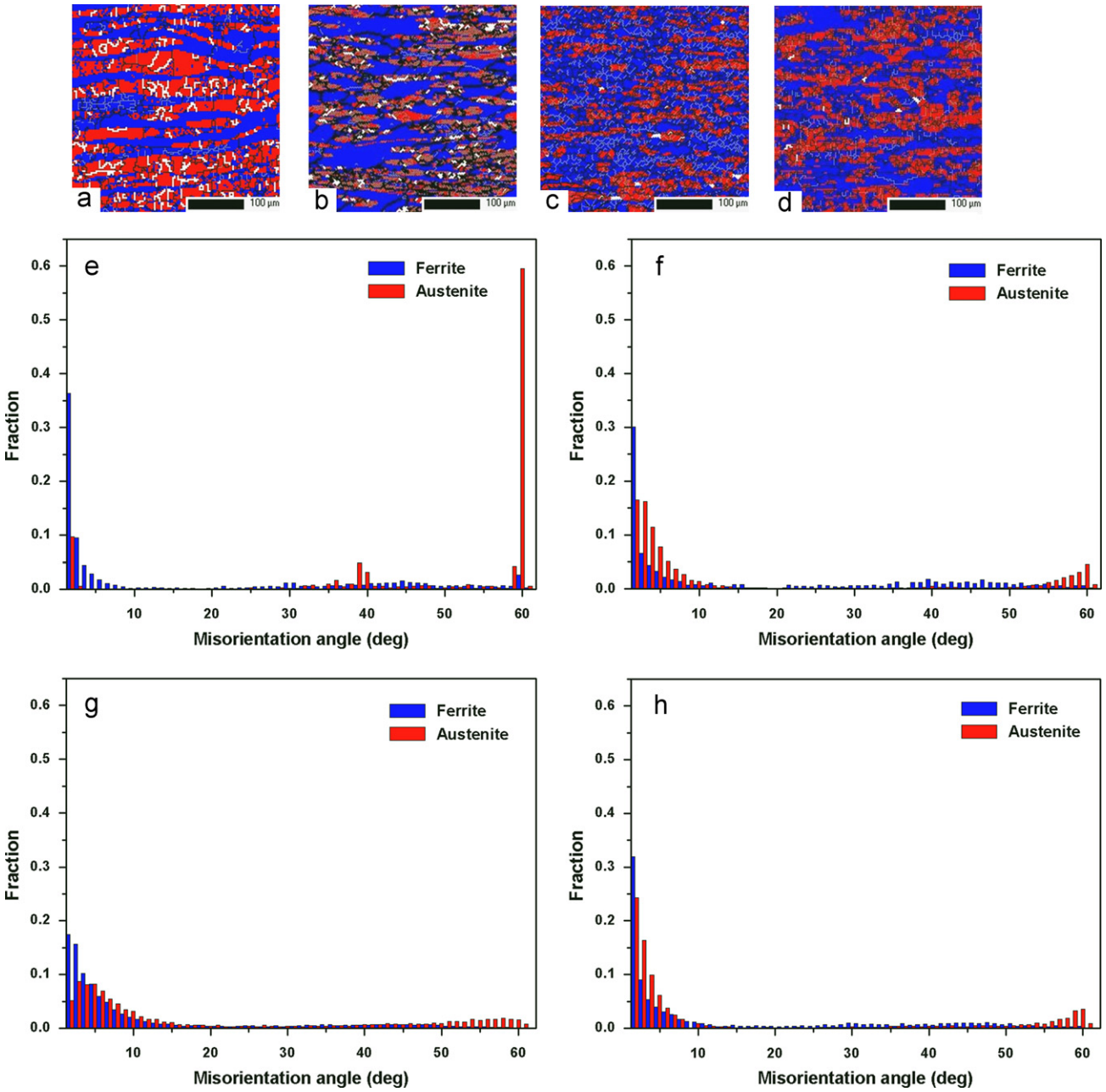

Fig. 3. EBSD maps (a, b, c, and d) and distributions of the adjacent grain misorientation angles (e, f, g, and h) at different strains during single- and multi-pass hot compressions: (a, e) $\varepsilon=0$; (b, f) $\varepsilon=0.4$, under multi-pass compression mode; (c, g) $\varepsilon=0.8$, under multi-pass compression mode and (d, h) $\varepsilon=0.8$, under single-pass compression mode.

and no apparent precipitation appears. As the starting material was forged, the austenitic islands were aligned before compression roughly parallel to the forging direction. These austenitic islands were composed of recrystallized grains containing large amounts of annealing twins. In the ferric phase, adjacent grain misorientation angles are mainly distributed in the range of 0°–15°, indicating that the majority of ferric grain boundaries are LAGBs. For the austenitic phase, approximately 10% of the adjacent grain mis orientation angles are distributed in the range of 0–15°, which are LAGBs (Fig. 3(e)). And approximately 60% of the high-angle boundaries displayed the first-order twin coincidence-site lattice (CSL) orientation relationship ∑3 (within a deviation of 2°) characterized by 60° rotation about the ⟨111⟩ axis. Around 5% of the boundaries appeared to correspond to the second-order twins represented by ∑9 (38.9°/⟨011⟩) CSL orientation relationship. A slight enhancement in the presence of the third-order twins, represented by ∑27a (31.6°/⟨011⟩) and ∑27b (35.4°/⟨012⟩) rotations, was also observed.

Under the multi-pass compression mode, after deformation to a strain of 0.4, the austenitic islands became more elongated and aligned in the rolling direction (Fig. 3(b)). In the ferric phase, LAGBs were still the majority. However, LAGBs in some areas were transformed into HAGBs, and subgrain structures began to form. Simultaneously, in the austenitic phase, LAGBs significantly increased, and most of the adjacent grain misorientation angles were distributed in the range of 0–15°. The originally sharp peak in the austenite misorientation distribution centered on the ideal ∑3 CSL orientation relationship became broader, the portion of the first-order twin boundaries decreased to approximately 5% and almost no indication of the enhanced presence of second-order twin boundaries was observed in the misorientation spectrum (Fig. 3(f)).

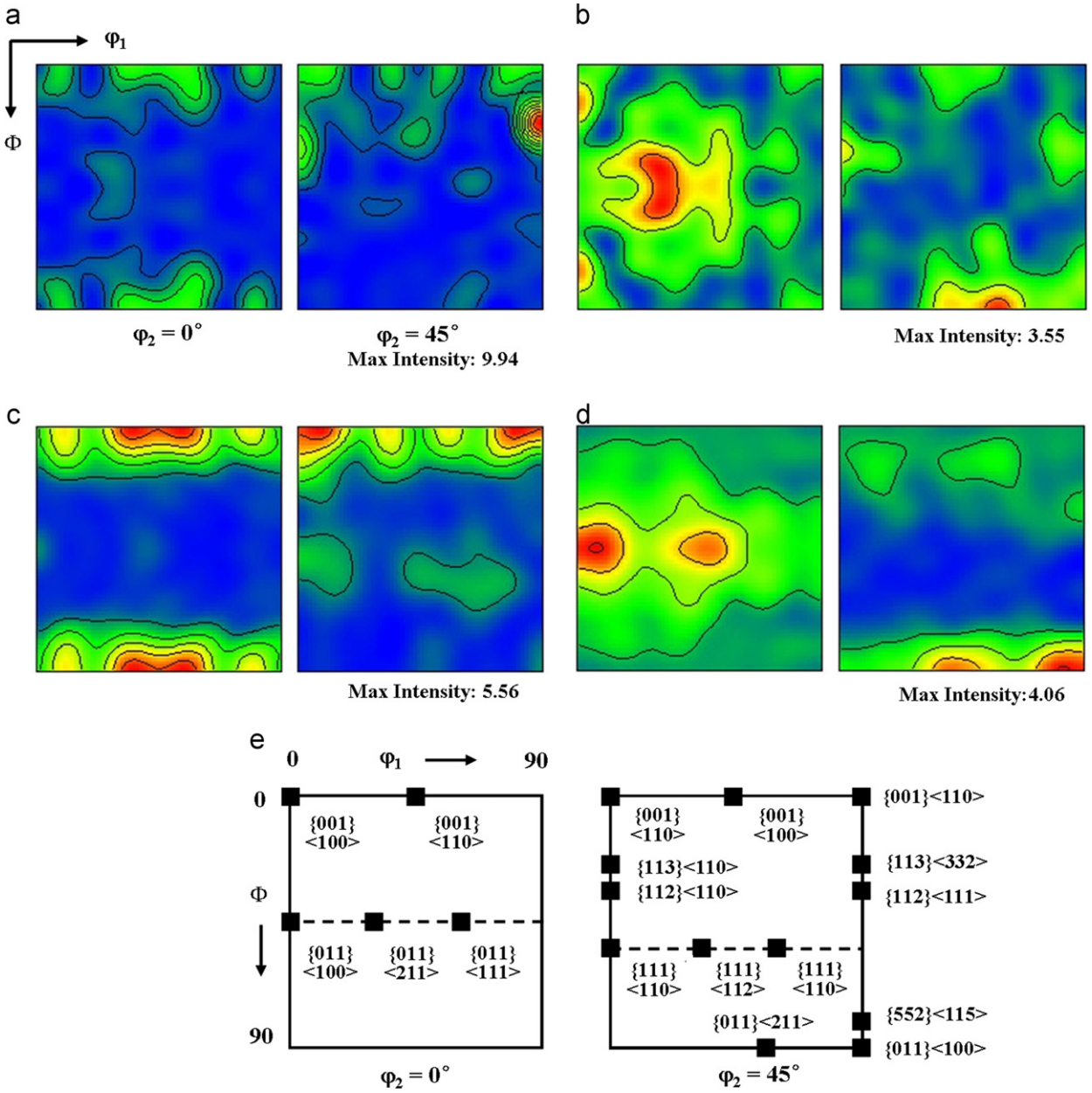

Fig. 4. EBSD technique determined ODF sections with constant φ_2 (0°, 45°) showing crystallographic textures of (a, c) ferric and (b, d) austenitic phases in the LDX 2101 after single- and multi-pass hot compressions: single-pass compression mode (a, b) and multi-pass compression mode (c, d); (e) schematics of the ideal texture components for φ_2=0° and φ_2=45° ODF sections.

After the strain was increased to 0.8, the austenitic islands became more elongated, possibly locally fragmented, and displayed a clear preferential alignment in the rolling direction (Fig. 3(c)). In the ferric phase, most of the LAGBs gradually transformed into HAGBs and formed fine ferric grains. Part of LAGBs began to transform into HAGBs in the austenitic phase. The broadening of the original $\sum 3$ peak in the austenitic misorientation distribution became more pronounced, and the portion of the first-order twin boundaries further decreased to only approximately 3% (Fig. 3(g)).

Fig. 3(d) and (h) shows the EBSD map and distribution of the adjacent grain misorientation angles under single-pass compression mode at 1100 °C and a strain of 0.8. Different from the multi-pass sample, the proportions of LAGBs among the grain boundaries in the ferric and austenitic phases were 15% higher, and the original $\sum 3$ peak in the austenite misorientation distribution was sharper under the single-pass hot compression mode.

These results indicate that during the hot deformation, the austenitic phase was relatively evenly distributed in the ferric matrix, and the ratio of the both phases did not significantly change. During the deformation process, the LAGBs in the ferric and austenitic phases gradually transformed into HAGBs. Under different deformation modes, some differences existed in the microstructure evolution features during the deformation process.

3.3. Crystallographic texture

Fig. 4 shows the orientation distribution function (ODF) sections of the ferric and austenitic phases in LDX 2101 after single- and multi-pass hot compressions under constant φ_2 (0°, 45°). Textures appeared with a marked intensity in the ferrite, mainly consisting of a sharp fiber (⟨110⟩//RD) spread from {001}⟨110⟩ to {112}⟨110⟩ and showing a maximum on the {001}⟨110⟩ orientation for both conditions (Fig. 4 (a, c)). An interesting feature is the weakness of the {111}⟨110⟩ orientation in single-pass sample, just like the rest of the γ-fiber components (Fig. 4(a)) which are usually the dominating textures for BCC metals after rolling and annealing.

In the austenitic phase, the main deformation rolling texture characteristics of FCC metals were observed (Fig. 4 (b, d)), such as brass ({011}⟨211⟩), copper ({112}⟨111⟩), and goss ({011}⟨100⟩) component. The presence of cube texture in the single-pass sample revealed that during hot compression, austenite recrystallized dynamically or meta-dynamically [9,10]. In addition, in the single-pass sample, the copper orientation shifted from its ideal position ($\varphi_1 = 90°$) to lower φ_1 values, indicating the deformation inhomogeneities (nonuniform deformation) like shear deformation and shear bands formation.

For the texture intensity, the ferric matrix had higher texture intensities than the harder austenitic phase. Under the two deformation modes, the texture intensities of the austenitic phase were similar, but texture intensity of the ferric phase under the multi-pass mode was much lower than that under the single-pass mode. This means that the texture intensities difference in the both phases was small under the multi-pass deformation mode.

4. Discussion

4.1. Microstructural evolution of the ferric phase

Fig. 3(a) and (c) shows that the grains of both phases were refined after hot compression processing. The average grain diameter has changed from 73 μm to 24 μm for ferric phase, and from 42 μm to 15 μm for austenitic phase. Generally, the refinement mechanism of ferric grain is the traditional discontinuous DRX (DDRX) and continuous DRX (CDRX) [11]. Traditional DDRX has an obvious grain nucleation process characterized by the "grain boundary protruding" phenomenon. Because this phenomenon was not observed in Fig. 3, DDRX refinement mechanism was excluded. Therefore, CDRX may be the reason for the grain refinement in the ferric phase.

The EBSD results show that many LAGB within the grains were formed in the early stage of deformation and that the LAGBs gradually transformed into HAGBs as the deformation process continued. This result is consistent with the occurrence of CDRX in the ferric phase reported by Hodgson, Chen and Sun et al. [12–14]. According to this mechanism, large fractions of mobile dislocations generated by deformation become continuously absorbed in the low-angle boundaries created by dynamic recrystallization processes at the early stages of straining, which gradually increases the mean misorientation angle and widens the misorientation spectra with increasing strain [6,12]. The above mechanism is generally characterized by the overall progressive refinement of subgrains, which is particularly pronounced during the initial stages of deformation. The subgrains become gradually converted to crystallites bounded partly by low-angle and high-angle boundary facets when straining continues to large strain levels. Locally, some fragments may become completely bounded by high-angle boundary segments, thus representing new recrystallized grains [13–15]. The above mechanism is generally associated with the development of a strong deformation texture. The higher misorientations and stronger textures observed in the ferric phase compared with the austenitic phase suggest that generally more strains are partitioned to the ferric phase than to the austenitic phase at a given nominal strain level. This finding agrees well with the observations reported by Akdut and Foct. [16].

4.2. Microstructure evolution of the austenitic phase

Similar to single-phase austenitic stainless steels, a large amount of annealing twins was observed in the austenitic phase of DSS after solution annealing [17,18]. During straining, the pre-existing annealing twin regions within the austenitic phase displayed a tendency to progressively rotate away from the ideal CSL orientation relationship. Fang et al. studied the typical TEM image of the austenitic phase in DSS, they found that twins were present in the austenitic phase, the twin boundaries were bent, and some dislocations occurred beside the austenitic twin boundaries [19]. The dislocations which meet the stringent conditions (specific slip plane, Burgers vector, shear stress and temperature) can directly pass through the twin boundaries [20,21]. The dislocations that cannot pass through the twin boundaries will interact with the twin boundary dislocation network, resulting in the disappearance of the $\sum 3$ twin boundary [17].

Similar to the softening mechanism in the ferric phase, LAGBs transformed into HAGBs in the austenitic phase (Fig. 3). This phenomenon was also reported in a previous study, wherein CDRX occurred in the austenitic phase of a 23Cr–5Ni–2Mn duplex stainless steel. Cizek and Wynne [6] have suggested that for DSS, limited austenitic grain boundaries and the presence of several ferric phases largely a effect the distribution of strain in the austenitic phase, causing the occurrence of CDRX in the austenitic phase.

4.3. Two-phase compatible deformation and effects of different deformation modes

The microstructure evolution of DSS in the hot deformation process was mainly affected by the strain distribution and deformation modes [22]. Compared with single-phase ferric or austenitic stainless steels, microstructure evolution during the high temperature deformation of DSS was very different as reflected by the flow curves and the EBSD analysis.

In the initial stage of deformation, the dislocation density of the ferric phase increased and caused work hardening. The strain was mainly distributed in the soft ferric matrix; thus the transfer of the strain to the austenitic phase through phase boundaries was delayed, thus preventing deformation continuity, and leading to "yield-like platform" softening phenomenon. This phenomenon is consistent with those reported by Jinmenze and Duprez [22,23]. As reduction increased, strain transferred from the ferric phase to the austenitic phase through phase boundaries to maintain the continuity of deformation. Because austenitic phase has a higher hardness, strain transfer increased in flow stress and caused hardening again. As the strain was further increased, CDRX was found to occur in the ferric and austenitic phases. Simultaneously, as the $\sum 3$ grain boundaries gradually disappeared in the austenitic phase, softening occurred again in the flow curve. During the hot deformation process, the coupling mechanism in microstructure evolution of both the phases determines the characteristics of the flow curve.

Under different deformation modes, some differences in the microstructure evolution features can be observed. This phenomenon is caused by the different softening mechanisms during single- and multi-pass hot compressions. Under the multi-pass hot compression mode, LDX 2101 underwent restoration through the mechanism of dynamic recrystallization. During the intervals of high-temperature deformation, three distinct softening mechanisms (i.e. static recovery, metadynamic recrystallization and static recrystallization) may occur [24]. Because the multi-pass sample suffered more softening, more LAGBs transferred into HAGBs in both the phases, which resulted in finer grains in both phases. These results indicate that the rolling process parameters such as the pass number and interval time could be adjusted during the hot rolling processing of LDX 2101 to optimize the microstructure of the rolled plate.

4.4. Crystallographic texture evolution

During the hot rolling process of LDX 2101, microstructure deformation, phase transformation and dynamic recrystallization occurred. Compared with single-phase stainless steels, the hot rolled texture was more complex in DSS.

For the ferric phase, at high temperatures, ferrite performed most of the deformation because it was the softer matrix phase. Under the hot rolling process, the austenitic phase textures were composed of two parts: deformation texture and recrystallization texture. The ferric phase textures were composed of three parts: deformation texture, recrystallization texture and phase transformation texture. Thus, the ferric phase texture was more complex and had higher intensity than the austenitic phase texture. During hot deformation, strain hardening, recrystallization and phase transformation alternatively occurred in the austenitic and ferric phases under different deformation modes, which caused the complexity and differences of the final textures [25].

Throughout the entire hot compression process, phase transformation continuously occurred in both the phases. At low reductions, the $\{113\}\langle 332\rangle$ texture in the ferric phase evolved from the $\{112\}\langle 110\rangle$ texture of the austenitic phase. This evolution is consistent with the K–S heredity relationship of the austenitic phase [26].

Under the two different deformation modes, an obvious difference in the ferric phase is the weakness of the γ-fiber components, indicating that the dynamic recrystallization was significantly suppressed in the ferric phase under the single-pass deformation mode. This phenomenon is because the multi-pass sample suffers more softening, leading to more recrystallization texture components in the multi-pass sample.

For the austenitic phase, the main part of the deformation rolling texture characteristics of FCC metals was observed (Fig. 4 (b, d)), including brass ($\{011\}\langle 211\rangle$), copper ($\{112\}\langle 111\rangle$), and goss ($\{011\}\langle 100\rangle$) components. Moreover, the presence of cube textures in the single-pass sample reveals that austenite recrystallized dynamically or meta-dynamically during hot compression [9]. Dynamic recrystallization and deformation were noticeable because of the RD-rotation of the cube orientation via the goss to the brass orientation, which is the ultimate deformation component in FCC materials with low SFC [10]. In addition, in the single-pass sample, the copper orientation shifted from its ideal position ($\varphi_1 = 90^\circ$) to lower φ_1 values, indicating the presence of deformation inhomogeneities like shear deformation and the formation of shear bands [7].

Under the two different deformation modes, the texture intensities of the austenitic phase were similar. However, the texture intensity of the ferric phase under the multi-pass mode was much lower than that under the single-pass mode. This means that the difference in texture intensities between both the phases was small under multi-pass deformation mode. This is due to the fact that under multi-pass deformation mode, more new recrystallized grains adopt random orientations during the pass intervals when rolling deformation is stopped but temperature is still high. Another reason for this phenomenon is that the average deformation temperature of the single-pass mode is higher, suggesting that the orientation rotations in the austenite and ferrite are easier during the single-pass mode than during multi-pass mode.

5. Conclusions

LDX 2101 was subjected to hot deformation under different deformation modes. The evolution of microstructure and crystallographic texture characteristics was studied using the EBSD technique. The following conclusions were drawn.

(1) During hot compression, as the reduction increased, the morphology of the austenitic phase changed from equiaxed to elongated ribbon structure, and the original $\sum 3$ grain boundaries gradually disappeared. The starting approximately equal volume fractions of austenite and ferrite remained unchanged, and typical continuous dynamic recrystallization occurred in both ferric and austenitic phases.
(2) A particular shape of flow curve, yield-like platform, was observed at the early stages of deformation, and the coupling mechanism of microstructure evolution during hot deformation determines the characteristic of flow curves. The proportions of LAGBs among the grain boundaries in the ferric and austenitic phases were higher, and the original $\sum 3$ peak in the austenitic misorientation distribution was sharper under the single-pass hot compression mode. This phenomenon is caused by different softening mechanisms during single- and multi-pass hot compressions.
(3) The α-fiber was the predominant texture in the ferric phase, and the multi-pass sample exhibited more developed γ-fiber components because it underwent more softening, which yielded more recrystallization texture components. Typical rolling textures of FCC metals were observed in the austenitic phase; the cube texture in the single-pass sample was an evidence of dynamic recrystallization processes. The texture intensity of the ferric phase was much larger than that of austenitic phase; the difference in the intensities between both the phases was smaller under multi-pass deformation mode.

Acknowledgments

The authors would like to thank Key Innovative Team for Magnetic Materials of Zhejiang Province and Zhejiang Provincial

Key Lab of Novel Materials for Information Technology, and College of Materials Science and Engineering, Shanghai Jiaotong University, for their great help with the EBSD studies. This work was supported by the Zhejiang Province Science and Technology Development Funds (2010C11SA48001).

References

[1] H.D. Solomon, T.M. Devine, Proceeding of Conference on Duplex Stainless Steels, ASM, Metal Park, OH, 1983, p. 693.
[2] A. Iza-Mendia, A. Pinol-Juez, J.J. Urcola, I. Gutierrez, Metall. Mater. Trans. A 29 (1998) 2975–2986.
[3] O. Balancin, W.A.M. Hoffmann, J.J. Jonas, Metall. Mater. Trans. A 31 (1999) 1353–1364.
[4] A. Dehghan-Manshadi, P.D. Hodgson, J. Mater. Sci. 43 (2008) 6272–6277.
[5] G.W. Fan, J. Liu, P.D. Han, G.J. Qiao, Mater. Sci. Eng. A 515 (2009) 108–112.
[6] P. Cizek, B.P. Wynne, Mater. Sci. Eng. A 230 (1997) 88–94.
[7] N. Jia, R.L. Peng, Y.D. Wang, X. Zhao, Mater. Sci. Eng. A 528 (2011) 3615–3624.
[8] M. Liljas, P. Johansson, H.P. Liu, C.A. Olsson, Steel Res. Int. 79 (2008) 466–473.
[9] G. Fargas, N. Akdut, M. Angland, A. Mateo, ISIJ Int. 48 (2008) 1596–1602.
[10] J. Hirsch, K. Lucke, M. Hatherley, Acta Metall. 36 (1988) 2863–2882.
[11] L.F. Li, W.Y. Wang, Z.Q. Sun, Metall. Mater. Trans. A 37 (2006) 609–617.
[12] B. Eghbali, A. Abdollah-Zadeh, H. Beladi, P.D. Hodgson, Mater. Sci. Eng. A 435–436 (2006) 499–503.
[13] J.L. Wan, X.J. Sun, J.L. Gu, N.P. Chen, Acta Metall. Sin. 35 (1999) 1031–1035.
[14] L.F. Li, W.Y. Wang, Z.Q. Sun, Acta Metall. Sin. 39 (2003) 419–425.
[15] V.Y. Gertsman, K. Tangri, Philos. Mag. A 64 (1991) 1319–1326.
[16] N. Akdut, J. Foct, Scr. Metall. Mater. 32 (1995) 109–114.
[17] H. Beladi, P. Cizek, P.D. Hodgson, Metall. Mater. Trans. A 40 (2009) 1175–1189.
[18] D. Jorge-Badiola, A. Iza-Mendia, I. Gutierrez, Mater. Sci. Eng. A 394 (2005) 445–454.
[19] Y.L. Fang, Z.Y. Liu, W.N. Zhang, G.D. Wang, Acta Metall. Sin. 46 (2010) 641–646.
[20] S. Poulat, B. Decamps, L. Priester, Philos. Mag. A 79 (1999) 2655–2680.
[21] L. Priester, Mater. Sci. Eng. A309-310 (2001) 430–439.
[22] J.A. Jinmenze, F. Carreno, O.A. Ruano, Mater. Sci. Technol. 15 (1999) 127–136.
[23] L. Duprez, B.C.D. Cooman, N. Akdut, Metall. Mater. Trans. A 33 (2002) 1931–1938.
[24] Z.Q. Sun, W.Y. Yang, J.J. Qi, A.M. Hu, Mater. Sci. Eng. A 334 (2002) 201–206.
[25] N. Akdut, J. Foct, Scr. Metall. Mater. 32 (1995) 103–108.
[26] R.K. Ray, J.J Jonas, Int. Mater. Rev. 35 (1990) 2–4.